

The variable stellar wind of Rigel probed at high spatial and spectral resolution^{★,★★,★★★}

O. Chesneau¹, A. Kaufer², O. Stahl³, C. Colvinter², A. Spang², L. Dessart⁴, R. Prinja⁵, and R. Chini^{6,7}

¹ Laboratoire Lagrange, UMR7293, Univ. Nice Sophia-Antipolis, CNRS, Observatoire de la Côte d'Azur, 06300 Nice, France
e-mail: Olivier.Chesneau@oca.eu

² European Southern Observatory, Alonso de Cordova 3107, Casilla 19001, 763-0355 Santiago, Chile

³ ZAH, Landessternwarte, Königstuhl 12, 69117 Heidelberg, Germany

⁴ Laboratoire d'Astrophysique de Marseille, Université de Provence, CNRS, 38 rue Frédéric Joliot-Curie, 13388 Marseille Cedex 13, France

⁵ Department of Physics & Astronomy, University College London, Gower Street, London, WC1E 6BT, UK

⁶ Instituto de Astronomía, Universidad Católica del Norte, Avenida Angamos 0610, Antofagasta, Chile

⁷ Astronomisches Institut, Ruhr-Universität Bochum, Universitätsstraße 150, 44801 Bochum, Germany

Received 22 October 2013 / Accepted 1 May 2014

ABSTRACT

Context. Luminous BA-type supergiants are the brightest stars in the visible that can be observed in distant galaxies and are potentially accurate distance indicators. The impact of the variability of the stellar winds on the distance determination remains poorly understood.

Aims. Our aim is to probe the inhomogeneous structures in the stellar wind using spectro-interferometric monitoring.

Methods. We present a spatially resolved, high-spectral resolution ($R = 12\,000$) K -band temporal monitoring of the bright supergiant β Orionis (Rigel, B8 Ia) using AMBER at the Very Large Telescope Interferometer (VLTI). Rigel was observed in the $\text{Br}\gamma$ line and its nearby continuum once per month over 3 months in 2006–2007, and 5 months in 2009–2010. These unprecedented observations were complemented by contemporaneous optical high-resolution spectroscopy. We analyse the near-IR spectra and visibilities with the 1D non-LTE radiative-transfer code CMFGEN. The differential and closure phase signals are evidence of asymmetries that are interpreted as perturbations of the wind.

Results. A systematic visibility decrease is observed across the $\text{Br}\gamma$ line indicating that at a radius of about $1.25 R_*$ the photospheric absorption is filled by emission from the wind. During the 2006–2007 period the $\text{Br}\gamma$ and likely the continuum forming regions were larger than in the 2009–2010 epoch. Using CMFGEN we infer a mass-loss rate change of about 20% between the two epochs. We also find time variations in the differential visibilities and phases. The 2006–2007 period is characterised by noticeable variations in the differential visibilities in Doppler position and width and by weak variations in differential and closure phase. The 2009–2010 period is much quieter with virtually no detectable variations in the dispersed visibilities but a strong S-shaped signal is observed in differential phase coinciding with a strong ejection event discernible in the optical spectra. The differential phase signal that is sometimes detected is reminiscent of the signal computed from hydrodynamical models of corotating interaction regions. For some epochs the temporal evolution of the signal suggests the rotation of the circumstellar structures.

Key words. techniques: high angular resolution – techniques: interferometric – stars: mass-loss – stars: individual: Rigel – stars: rotation – circumstellar matter

1. Introduction

The discovery of systematic, patterned variability in the stellar winds of luminous hot stars is important for our understanding of wind dynamics and stellar structure. Numerous time resolved observations of O stars like the FEROS campaigns on HD 152408 (O8 If) (Prinja et al. 2001) and particularly the IUE MEGA campaign on HD 64760 (B0.5 Ib) (Prinja et al. 1995; Massa et al. 1995) and on ζ Puppis (O4 I(nf)) (Howarth et al. 1995) as well as the extended optical HEROS campaigns over typically 100 consecutive nights on late B- and

early A-supergiants (Kaufer et al. 1996a,b, 1997) and early B-hypergiants (Rivinius et al. 1997) have led to a radically new view of hot-star winds. These campaigns have shown that the winds of hot stars are continuously variable on timescales associated with processes on the stellar surface. Consequently, the steady state, spherically symmetric descriptions usually used to model and interpret stellar wind diagnostics (see e.g. Przybilla et al. 2006) can only provide some sort of mean representation of these outflows. One of the essential questions for understanding the nature and origin of the wind variability is its connection to the stellar photosphere. For OB-type supergiants like HD 64760, HD 152408, ζ Puppis, and the BA-type supergiants like Rigel (β Orionis, B8 Ia) and Deneb (α Cygni, A2 Ia), cyclic modulation of the stellar wind plays an important role. Obviously, the winds are modulated by a mechanism related to the photospheric rotation, presumably patches on the stellar surfaces produced either by non-radial pulsation (NRP) patterns (Lefever et al. 2007) or magnetic surface structures (spots or extended loops) (Schnerr et al. 2008). The spatial structures in the photospheres locally

* Based on observations collected at the European Southern Observatory (ESO Programmes 078.D-0355 and 084.D-0393) and at the Observatorio Cerro Armazones (OCA) in Chile.

** Appendices are available in electronic form at <http://www.aanda.org>

*** Reduced BES0 data are only available at the CDS via anonymous ftp to cdsarc.u-strasbg.fr (130.79.128.5) or via <http://cdsarc.u-strasbg.fr/viz-bin/qcat?J/A+A/566/A125>

change the lower boundary condition of the stellar wind, which in turn can cause localised structural changes in the wind. These structural changes modulate the observed stellar wind profiles as they are dragged through the line of sight to a distant observer by underlying rotation of the star. For the prototypical B0.5 Ib supergiant HD 64760, Cranmer & Owocki (1996) have modelled such structured winds in the context of corotating interaction regions (CIRs). Kaufer et al. (2006) have presented strong evidence that multiperiodic NRPs are the direct source of the regularly spaced wind structures in this star. Stellar activity has deep consequences for the interpretation of the spectra of hot massive stars, the macroturbulent broadening being a good example of such an issue (Simón-Díaz et al. 2010; Shultz et al. 2011; Aerts et al. 2009; Dessart & Owocki 2002). Stochastic variability is also present related to small-scale clumping of the radiative wind (Dessart & Owocki 2005). Clearly, to make progress understanding these new phenomena and their impact on the fundamental process of mass-loss via stellar winds – and therefore on stellar evolution scenarios –, the mechanism(s) responsible for dividing the stellar wind into structured low and high density regions must be determined.

Recent advances in optical interferometry open up a completely new window for the exploration of the wind structures of hot supergiants. For the first time, *direct* measurements of the spatial extension of the circumstellar structures as function of wavelength across a wind-sensitive spectral line like Br γ become feasible. Currently only two instruments provide spectrally dispersed interferometric observables with a spectral resolution power larger than $R = 10\,000$ and a spatial resolution around a milliarcsecond: the VEGA visible recombiner at CHARA (Mourard et al. 2009) and the AMBER near-IR recombiner (Petrov et al. 2007) at the VLTI. These instruments are well suited to study the wind activity of the brightest BA supergiants in our vicinity in wind-sensitive spectral lines such as H α or Br γ (Chesneau et al. 2010). Deneb and Rigel were observed by Chesneau et al. with VEGA in 2009. The extension of the H α line forming region of both stars was accurately measured and compared with CMFGEN models (Hillier & Miller 1998). Moreover, clear signs of activity were observed in the differential visibility and phases. These pioneering observations, based on recombination of only two telescopes at a time were limited but show the path for a better understanding of the spatial structure and temporal evolution of localised ejections using optical interferometry.

The bright late-type B supergiant Rigel (= β Orionis = HD 34085) (B8 Ia) with a K -band magnitude of 0.2 and a stellar diameter of 2.76 mas (Aufdenberg et al. 2008) is an ideal target for a more in-depth spectro-interferometric study of the variability of hot supergiants. The photosphere and wind variability of Rigel have been extensively studied by Kaufer et al. (1996a,b, 1997) by means of spectroscopic time series in the optical. The red-to-blue variations in the H α emission and absorption features are reminiscent of the variations in Be-stars and indicate the presence of circumstellar structures preferably localised in the equatorial plane and close to the stellar surface between 1 and 2 stellar radii. The timescales of the variations are of the order of several weeks to months and compatible with the estimated stellar rotation period of 100 days considering that several active regions are present at the same time. Extreme events like the high-velocity absorptions (HVA; Kaufer et al. 1996a) have indicated that circumstellar structures can be stable for several rotational cycles. Temporal variations in the near-infrared regime remain to date mostly unexplored. However, the Br γ line is expected to play an important role in this respect since the

near-IR continuum is formed closer to the wind launching region near the photosphere. Therefore, near-infrared lines such as Br γ are expected to provide complementary information to the well-established optical spectral variability.

In this work we report on a more ambitious extensive spectro-interferometric monitoring of Rigel using the high-spectral resolution mode of AMBER. The AMBER observations were collected in two observing campaigns in 2006–2007 and 2009–2010 covering the full observing season of Rigel over some five months each. The AMBER observations were complemented by quasi-simultaneous high-spectral resolution optical monitoring. Interestingly, the 2009–2010 AMBER observations performed from the modified Julian date (defined as Julian date – 2 400 000.5, hereafter MJD) MJD 55 139 until MJD 55 300 partially overlap with the global Rigel monitoring campaign – known as the “Rigel-thon” – involving long-term spectroscopic monitoring, Microvariability and Oscillations in STars (MOST) space photometry, and spectropolarimetry (Moravveji et al. 2012a; Shultz et al. 2011). Owing to the brightness of the star, stringent constraints on the possible existence of magnetic field were provided up to a limit of the individual measurements as low as 13 G and exclude large dipolar fields in the range of 20–50 G. The MOST data also fostered some theoretical developments on the asteroseismology of this star (Moravveji et al. 2012b).

The paper is structured as follows. In Sect. 2 we present the optical and near-infrared spectroscopic and interferometric data and their reduction. Section 3 analyses the available interferometric continuum information. Section 4 describes the spectral variability in the H α and Br γ lines using time series of spectra of Rigel obtained for the first time quasi-simultaneously in the optical and the near-infrared. In Sects. 5 and 6 the interferometric observables visibility and phase are analysed to describe the size and structure of the Br γ line-forming region and the observed possibly rotating circumstellar structures. After a summary of the results and a discussion in Sect. 7 we close with our conclusions in Sect. 8.

2. Observations and data reduction

2.1. Optical spectroscopy

The optical observations of Rigel during the 2006–2007 campaign were carried out with the high-resolution echelle spectrograph FEROS (Kaufer et al. 2000) at the ESO/MPG 2.2-m telescope at La Silla. A total of 183 spectra with a resolving power of $R = 48\,000$ and a wavelength coverage of 3600–9200 Å were collected in 20 nights between October 3, 2006, and March 31, 2007. For the 2009–2010 campaign the BESO (Bochum Echelle Spectrograph for OCA) spectrograph at the 1.5-m Hexapod-Telescope at the Observatorio Cerro Armazones (OCA), Chile, was used. BESO is basically identical to FEROS and was built by the Ruhr-Universität Bochum and Landessternwarte Heidelberg (Fuhrmann et al. 2011). A total of 79 spectra were obtained between October 6, 2009, and April 7, 2010. Table A.1 provides the dates of the individual observations. FEROS obtained sequences of up to 20 spectra of 1 s exposure time to achieve a typical signal-to-noise ratio of 400 per combined spectrum (at 5400 Å). BESO obtained a typical signal-to-noise ratio of 250 per spectrum from single 100 s exposures. Flatfield and wavelength-calibration exposures have been obtained with the instrument-internal halogen and thorium-argon lamps at the beginning of the respective nights. All spectra have been reduced semi-automatically with ESO-MIDAS using

the dedicated FEROS context as described e.g. in [Stahl et al. \(1999\)](#). All spectra have been reduced to barycentric velocities and have been normalised to the stellar continuum using the very stable instrument response curve and low-order fits to clean stellar continuum points. Throughout this paper, all velocities are given with respect to the laboratory wavelengths of the corresponding lines of interest. For this purpose the wavelengths of the respective lines have been corrected by a systemic velocity of $v_{\text{sys}} = +18 \text{ km s}^{-1}$ for Rigel ([Kaufer et al. 1996b](#)).

2.2. Near-IR spectroscopy and interferometry

Rigel was observed at the ESO Paranal Observatory with the Astronomical Multi BEam Recombiner (hereafter AMBER), the near-infrared instrument of the VLTI ([Petrov et al. 2007](#)). AMBER operates in the *J*, *H*, and *K* bands with spectral resolutions of 35, 1500, and 12000, combining either three 8.2-m Unit Telescopes (UTs) or 1.8-m Auxiliary Telescopes (ATs). The observations were carried out on a monthly basis in two campaigns, the first from December 30, 2006, to March 8, 2007, and the second from November 4, 2009, to April 13, 2010. The observations were performed in the high spectral resolution mode ($R = 12\,000$, i.e. 25 km s^{-1} per 2-pixel resolution element) and the spectral range of $2.147\text{--}2.197 \mu\text{m}$ in order to resolve the observable velocity fields of Rigel in the Bry line at $2.1661193 \mu\text{m}$. The 2006–2007 campaign was performed with the UTs due to the sensitivity limitations of AMBER in high-resolution mode at that time. Significant improvements of the AMBER instrument allowed us to move in 2009 from the UTs to the ATs which then provided data of comparable quality. The interferometric observations were carried out by ESO in service mode. Because of the significant investment of VLTI observing time to obtain an interferometric time series of Rigel over a complete observing seasons from October to March, the frequency of observations was limited to one measurement (i.e. one “triplet” of baselines) per month – despite the known faster variability timescales of Rigel’s circumstellar environment. Some of the monthly measurements were performed at several days interval, implying that the atmospheric conditions specifically described to perform these observations optimally were not met and that the first dataset of such consecutive observations is of worse quality. However, these datasets were still analysed in the same way to test the errors and biases that can be expected from the data reduction. The log of the AMBER observations of Rigel has been compiled in [Table A.2](#).

AMBER records spectrally dispersed fringes on the detector and therefore provides wavelength-dependent measurements of the size, shape, and with sufficient spectral resolution, also the kinematics of the source corresponding to about eight independent spectral channels through the line. Three telescopes were systematically recombined, providing a data set consisting in three spectra, three dispersed visibilities, three differential phases, as well as one dispersed closure phase. The visibility is the normalised amplitude of the Fourier transform of the intensity distribution of the stellar source in the plane of the sky from which information on the size and shape of the object can be retrieved through some model-fitting analysis. We note that no image inversion is possible with this very limited dataset.

The atmospheric turbulence blurs the fringes at a fast rate so that it is not possible to measure a phase signal directly for each baseline, but the three telescope recombination provides two observables, the differential and closure phase that can be related to the phase of the source. The differential phase represents the wavelength-dependent phase of the source relative to

a reference channel. The reference channel is dominated by the continuum signal and the differential phase should consequently be observed with a mean value of zero degree. Strong departures from this mean value may be observed at some spectral channel centred in a line, indicating that the line-forming region at this velocity channel is offset with respect to the continuum. The closure phase is the sum of the phases around a closed triangle of baselines (i.e. $\phi_{12} + \phi_{23} + \phi_{31}$). This quantity is theoretically not affected by the atmospheric turbulence and the value for a spherical source should be zero. A systematic departure at the level of a few degrees from this value is observed due to instrumental defects that affect similarly the science and calibrator sources. After removal of this bias, a detected non-zero closure phase can be interpreted as an evidence of the asymmetrical nature of the source.

Observations of Rigel were systematically performed together with the observations of a calibrator to allow us to correct for the instrumental transfer function and other biases to the visibilities and the closure phases. Finding a good calibrator under these constraints of observation is difficult. Rigel is a bright, nearby late-B supergiant exhibiting a limited apparent angular diameter given the AMBER and VLTI spatial resolution. A good calibrator would have been a smaller source with a similar flux, that is, an even earlier source, moreover located at the immediate vicinity of Rigel. The calibrator 31 Ori (HD 36167) is a K5 III giant and was primarily chosen due to its brightness ($K = 0.8$ versus $K = 0.2$ for Rigel). Since the estimated angular diameter of 31 Ori is $3.56 \pm 0.06 \text{ mas}$ ([Bordé et al. 2002](#)) and therefore slightly larger than the one of Rigel, the accuracy of the absolute visibility calibration remains limited. However, such a measurement is not the main goal of this study.

The data was processed with the standard AMBER data reduction software (hereafter AMBER DRS, `amdlib` 2.2, see for instance [Tatulli et al. 2007](#)). Some procedures were developed to clean the data that are now inserted by default in the latest version `amdlib` 3 (better detector cosmetics). The best frames with $S/N \geq 1$ were selected and frames affected by high piston excluded.

In this correction process, realistic error estimates were derived from the data, including the uncertainties on the calibration stars diameters, the instrument and atmosphere transfer function instabilities and the fundamental noises. The study of the transfer function showed that V^2 uncertainties were often as large as 10–15%. Therefore, in the following only differential observables are used in the interferometric analysis. The data from the UTs are heavily affected by vibrations of the optical surfaces in the optical train that decrease significantly the level of the transfer function. In addition, the data recorded during the 2006–2007 campaign are affected by a time and wavelength dependent, high-frequency beating in the spectra, raw visibilities, differential phases, and closure phases. This Fabry-Perot effect has been identified to be caused by an optical component in the AMBER instrument. A Fourier transform of the observable quantities shows that at first order the beating is periodic. The data were corrected by suppressing the periodic peak in the Fourier domain. This correction removes the majority of the beating effect from the data. The zeropoint of the AMBER wavelength scale is not stable and drifts with time. To obtain an accurate wavelength calibration of the AMBER data, the spectral shifts were measured relative to two telluric water lines at 2.163477 and $2.168687 \mu\text{m}$ ([Rothman et al. 1992](#), HITRAN) that bracket the Bry line. The result of the correction is shown in [Fig. 1](#) for Rigel and 31 Ori in comparison to a convolved telluric K-band spectrum from Kitt Peak Observatory. The wavelength

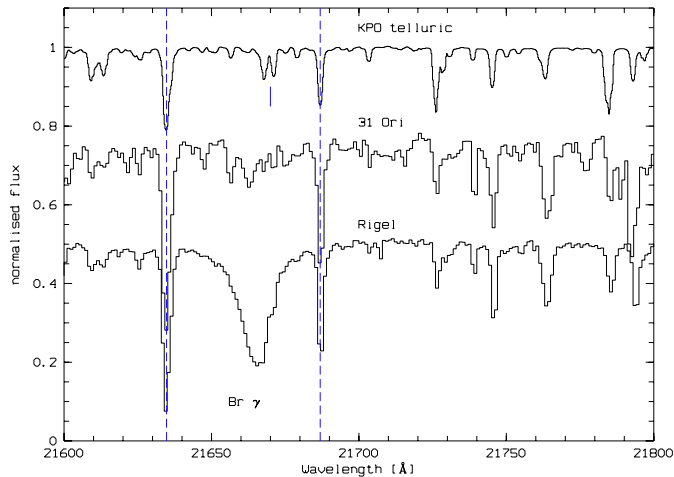


Fig. 1. Wavelength calibration of the AMBER observations. A telluric spectrum from the Kitt Peak Observatory (KPO) is shown in comparison with AMBER spectra of Rigel and 31 Ori around the Br γ line. The dashed vertical lines indicate the positions of the two telluric lines used as wavelength reference. The telluric line doublet at 2.1670 μm seen in the KPO spectrum does not feature in the 31 Ori spectrum. Therefore, the Br γ line profile of Rigel is bona fide undisturbed by telluric lines.

calibration error on the reduced AMBER data is estimated to be $\Delta\lambda = 1 \times 10^{-4} \mu\text{m}$ corresponding to less than 15 km s^{-1} . The spectral resolving power is measured from unblended telluric lines with 25 km s^{-1} equivalent to $R = 12\,000$. Eventually, all wavelength scales have been reduced to barycentric velocities and corrected by the systemic velocity $v_{\text{sys}} = +18 \text{ km s}^{-1}$ of Rigel.

3. Continuum information

At the HIPPARCOS distance of $d = 237_{-38}^{+57} \text{ pc}$, the radius of Rigel is $70 R_{\odot}$, and at the distance $d = 360 \text{ pc}$ adopted by Przybilla et al. (2006)¹, this corresponds to $106 R_{\odot}$. The width of the Br γ line forming region can be estimated to be $15\text{--}25 R_{\odot}$.

The absolute visibilities of AMBER are not accurate enough to provide strong constraints on the angular diameter. As a result of the high spectral resolution of the data only a narrow spectral band is covered limiting the range of spatial frequencies for each observation. However, given the comparatively large number of independent visibility measurements in our data set the respective angular diameters have been determined with some statistical significance: from the good quality data of the 2009–2010 campaign the angular diameter of Rigel in the K -band is estimated with a mean of $2.77 \pm 0.08 \text{ mas}$ and a median of 2.79 mas . The lower quality data of the 2006–2007 campaign provided an angular diameter systematically larger with a $3.01 \pm 0.28 \text{ mas}$ and a median value is 2.94 mas (this is due to one bad measurement).

The errors are estimated from the standard deviation of the diameter measurements performed at each date of observation but do not take into account the systematic bias introduced by the calibrator 31 Ori. It is not excluded that a true variability of the apparent diameter of the source may contribute to this scatter, since the Br γ line-forming regions seems also larger during 2006–2007 (see following section). The 2009–2010 results are consistent with the IONIC measurement at the VLTI

¹ We note however that they make use of the biased value of Hanbury Brown of 2.55 mas , leading to an estimate of $99 R_{\odot}$.

of $2.8 \pm 0.1 \text{ mas}$ (LeBouquin et al. 2004) and with the best estimate to date of $2.76 \pm 0.05 \text{ mas}$ from FLUOR at CHARA using K -band measurements with baselines reaching up to 300 m (Aufdenberg et al. 2008). The 2006–2007 and 2009–2010 continuum closure phases are compatible with a value of zero. No significant departure of the continuum closure phase averaged over the available spectral band is observed. The 2009–2010 continuum closure phases range from $-6.1 \pm 3.9^{\circ}$ to $2.4 \pm 2.9^{\circ}$, with a mean value of -0.7° and a median of -0.2° . The standard deviation of the closure phase is 1.8° , the median value 1.4° . The 2006–2007 continuum closure phases have a mean value of $0.9 \pm 2^{\circ}$ and a median of 1.1° .

4. Spectral time series information

4.1. $H\alpha$ and Br γ time series

The $H\alpha\lambda 6562.818 \text{ \AA}$ and Br $\gamma\lambda 21661.19 \text{ \AA}$ recombination lines are the most sensitive lines accessible to optical and near-infrared high-resolution spectrographs and interferometers like FEROS/BESO and AMBER to probe circumstellar material close to the stellar photosphere of Rigel. The complex variability of the circumstellar environment has been documented by Kaufer et al. (1996b) through extensive monitoring of the $H\alpha$ -line variability and was interpreted as rotational modulation of the lower wind regions of the star by complex circumstellar structures. No corresponding data sets existed so far in the near infrared. The AMBER spectro-interferometric monitoring presented in this work allows us, for the first time, to compare time series of $H\alpha$ and Br γ spectroscopic line profiles of Rigel.

Figure 2 shows a selected subset of the available $H\alpha$ and Br γ time series. All available Br γ spectra taken during the 2009–2010 campaign are shown as difference of the recorded Br γ spectra and an artificial Gaussian photospheric line profile to make possible more direct comparison of the Br γ line profiles with $H\alpha$. The photospheric line profile was constructed from a Gaussian profile with a full width at half maximum (FWHM) of 22.8 km s^{-1} to match the wings of the Br γ profiles and a central depth of 0.8 times the continuum to reproduce the typical central depth of the $H\alpha$ line profiles. For a more direct comparison of Br γ and $H\alpha$ only the $H\alpha$ spectra closest in time to the Br γ spectra are shown (the complete $H\alpha$ and Br γ time series from the 2006–2007 and 2009–2010 campaigns are shown in Figs. B.1, B.2, C.1, and C.2 in the Appendix and are discussed in the following sections).

Figure 2 shows that the AMBER spectra despite their considerably lower spectral resolution than the BESO spectra mostly resolve the line-profile variations displayed in the Br γ line profile. It also suggests that the line-profile variability observed in $H\alpha$ and Br γ are qualitatively very similar. Both $H\alpha$ and Br γ display red-to-blue variations in emission and absorption features which are reminiscent of the variations in Be-stars and indicate the presence of circumstellar structures in the equatorial regions of the star as established earlier from extended optical time series by Kaufer et al. (1996b). The line-profile variability is primarily caused by variable additional emission superimposed to the underlying photosphere – wind profiles. However, it is also clear that the Br γ line profiles do not necessarily match the corresponding $H\alpha$ profile: while $H\alpha$ and Br γ often appear very similar with matching emission and absorption components like at MJD 55 217 and MJD 55 267, the profiles appear with opposite emission and absorption components at MJD 55 238. A closer inspection of the full time series in Figs. C.1 and C.2 does not reveal any obvious time delay between the evolving line profiles

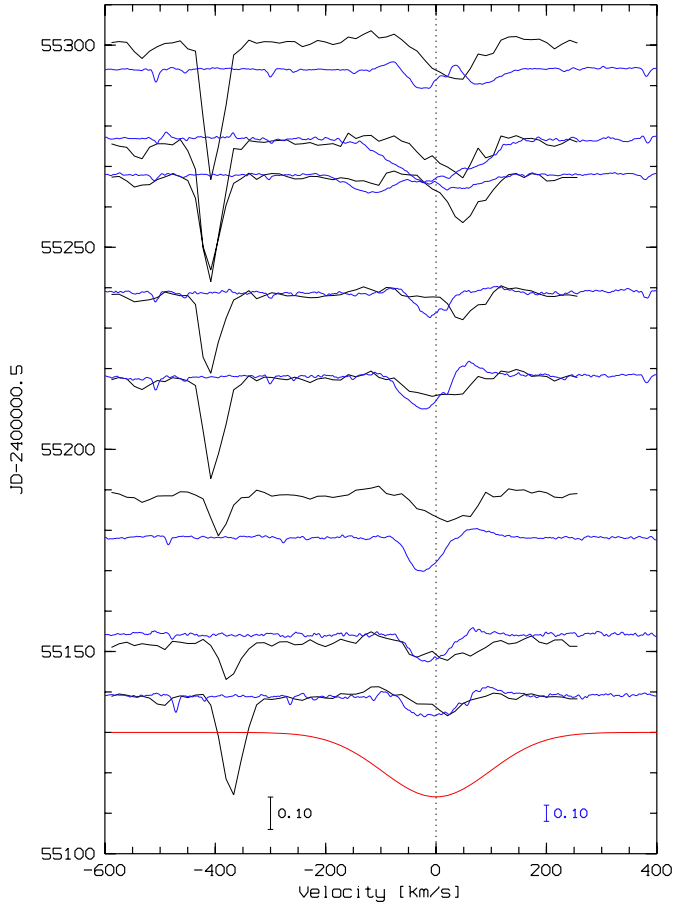


Fig. 2. 2009–2010 Bry (black) and $H\alpha$ (blue) time series of Rigel. The Bry spectra are shown as the difference to an artificially created photospheric spectrum shown at MJD 55 130 (red). For $H\alpha$ only the spectra taken closest in time to the Bry spectra are shown. The normalised flux scale for Bry is enlarged by a factor of two relative to the one of $H\alpha$ to match the strength of profile variability of the two lines. The strong telluric water absorption line at -400 km s^{-1} is not resolved and provides an estimate of the spectral resolution of the AMBER spectra around Bry. The complete 2009 time series are shown in Figs. C.1 and C.2.

of $H\alpha$ and Bry as it could be expected from features propagating through the photosphere – wind transition zone at the base of the wind. It is therefore concluded that the $H\alpha$ and Bry lines are both probing well the photosphere – wind transition zone at the base of the wind of Rigel but either at different stellar radii and volumes or through different (local) line-formation processes (see Fig. 4).

4.2. 2006–2007 campaign

The $H\alpha$ time series from the 2006–2007 campaign is shown in Fig. B.1. The $H\alpha$ profiles display most of the time a double-peaked profile with blue and red emission peaks with maxima at -70 km s^{-1} and $+70 \text{ km s}^{-1}$, respectively, i.e. at velocities higher than the estimated projected equatorial rotation velocity of $v \sin i = \pm 36 \text{ km s}^{-1}$. The most notable feature of the time series is the blue shifted high-velocity absorption (HVA) at MJD 54 037 with a blue-edge velocity of the absorption feature of -390 km s^{-1} and a maximum depth of 12% of the continuum at -127 km s^{-1} . HVAs have been observed in Rigel and other BA supergiants before and were first described in Kaufer et al. (1996b). The 2006 HVA is only recorded by one single

FEROS spectrum with the previous spectrum at MJD 54 019 and the next at MJD 54 071, i.e. several weeks before and after the event. $H\alpha$ displays unusually strong inverse P-Cygni profiles at MJD 54 019 before the event and between MJD 54 087 and MJD 54 117 after the event, the latter with a strong inverse P-Cygni profile slowly developing back into the more regular double-peaked profile as described above. Because of the sparse sampling of the 2006–2007 time series no clear links can be established between the sequence of line profiles (inverse P-Cygni profile, HVA, decaying inverse P-Cygni profile, double-peaked profile). The even fewer Bry spectra recorded with AMBER and shown in Fig. B.2 do not allow us to fill the time gaps. Unfortunately, no AMBER spectra were recorded near the HVA event. The Bry spectra between MJD 54 099 and 54 108 map the inverse P-Cygni profiles in $H\alpha$ by showing a red-shifted absorption core of the line profile. Subtracting the artificial photospheric profile as described above reveals inverse P-Cygni profiles in Bry, too. So far, the best-documented HVA events of Rigel in 1993 and 1994 (Figs. 1 and 2 in Kaufer et al. 1996b) also indicate the appearance of inverse P-Cygni profiles before and after the observation of HVAs. In the 1993 event the inverse P-Cygni profile was recorded some 19 days before the deepest HVA profile, i.e. with the same time difference as in 2006. The blue-edge velocity of -390 km s^{-1} observed in the 2006 HVA is considerably higher than the ones observed in 1993 and 1994 with -238 km s^{-1} and -278 km s^{-1} , respectively, and considerably higher than the terminal wind velocity estimated from UV spectra of the Mg $\text{II} \lambda\lambda 2795, 2803$ lines with a lower limit of -229 km s^{-1} . Gilheany (1991) reported on discrete absorption components extending to -400 km s^{-1} in Rigel.

4.3. 2009–2010 campaign

The $H\alpha$ and Bry time series from the 2009–2010 campaign are shown in Figs. C.1 and C.2. The $H\alpha$ profiles display from MJD 55 110 to MJD 55 240 double-peaked profiles with red-to-blue variations in emission and absorption features as most commonly seen in Rigel. At MJD 55 264 an absorption feature with a blue-edge velocity of -200 km s^{-1} becomes discernible at blue-shifted velocities and rapidly develops into a broad absorption feature crossing the line profile from blue to red within the next two weeks reaching a red-edge velocity of $+100 \text{ km s}^{-1}$ at MJD 55 280. Interestingly, Bry already shows red-shifted absorption at $+50 \text{ km s}^{-1}$ at MJD 55 238 (Figs. C.2 and 2). The red-shifted absorption even increased in strength (depth) by MJD 55 267 and is still visible at MJD 55 275.

5. Differential visibilities and the Bry line forming-region

Figures B.3, and C.3–C.4 show the measured differential visibilities across the Bry line from the 2006–2007 and 2009–2010 data set, respectively. For each observation three differential visibilities are shown corresponding to the three baselines formed by the ATs. Given the uncertainties of the continuum visibility measurements with AMBER, the continuum visibilities are set according to a fixed value of 2.76 mas for the angular diameter of the photosphere of Rigel (Aufdenberg et al. 2008). The interpretation of the interferometric observables (visibilities and phase) requires the support by theoretical models of the stellar photosphere and wind. The stellar parameters used for the model calculations are taken from Przybilla et al. (2006) and Markova et al. (2008). The MgII resonance lines suggest terminal wind

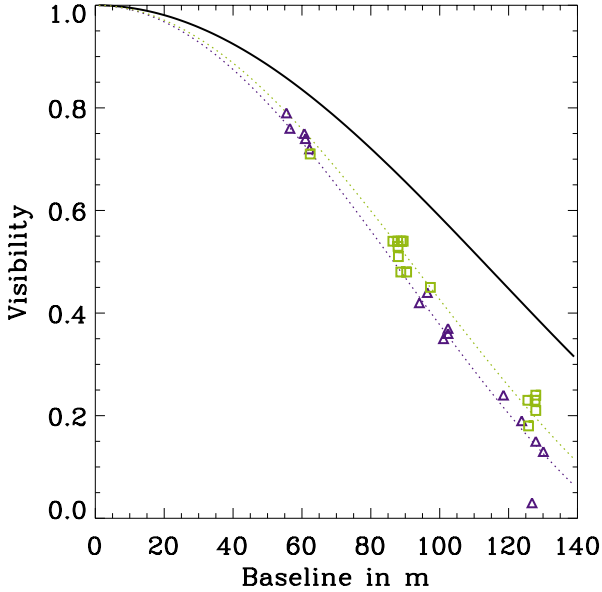


Fig. 3. Depth of the differential visibility curves for Rigel referenced to the uniform-disk diameter curve, corresponding to 2.76 mas. The AMBER measurements of the differential visibility obtained in the core of the line are indicated by triangles (2006–2007 campaign) and squares (2009–2010 campaign). A fit of these values by two uniform-disk diameter curves provides with angular diameters of 3.58 ± 0.04 mas and 3.45 ± 0.04 mas, for 2006–2007 and 2009–2010, respectively.

Table 1. CMFGEN parameters for Rigel.

Parameter	Value
Luminosity L_*	$2.79 \times 10^5 L_\odot$
Terminal wind velocity v_∞	300 km s^{-1}
Stellar radius R_*	$115 R_\odot$
Mass loss \dot{M}	1, 2, 4, 6, 7, 8, 9, 10 $\times 10^{-7} M_\odot \text{ yr}^{-1}$
Effective temperature T_{eff}	12 000 K
Filling factor	10%
Composition	solar

speeds of $\sim 230 \text{ km s}^{-1}$ for Rigel and the projected rotational velocity is low, at about $36 \pm 9 \text{ km s}^{-1}$ (Kaufer et al. 1996b). All spectra and the dispersed visibilities of the Bry line are computed for a spectral resolution $R = 12\,000$.

The modelling approach is extensively described in Chesneau et al. (2010). We used a similar modelling approach but with the model parameters listed in Table 1. The mass-loss rate was varied to cover the values 1, 2, 4, 6, 7, 8, 9, and $10 \times 10^{-7} M_\odot \text{ yr}^{-1}$. The radiative-transfer calculations were carried out with the line-blanketed non-LTE model-atmosphere code CMFGEN (Hillier & Miller 1998; Dessart & Hillier 2005), which solves the radiation-transfer equation for expanding media in the co-moving frame, assuming spherical symmetry and steady-state, and under the constraints set by the radiative-equilibrium and statistical-equilibrium equations. It treats line and continuum processes and regions of both small and high velocities (small and high velocities relative to the thermal velocity of ions and electrons). Hence, it can solve the radiative-transfer problem for both O stars, in which the formation regions of the lines and continuum extend from the hydrostatic layers out to the supersonic regions of the wind, and Wolf-Rayet stars, in which lines and continuum both originate in regions of the wind that may have reached half its asymptotic velocity.

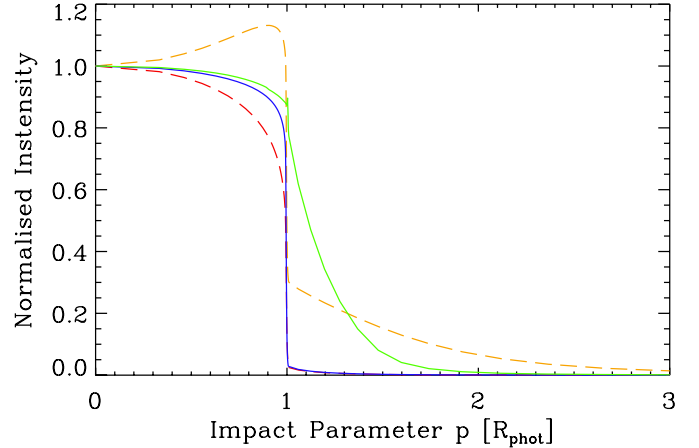


Fig. 4. A CMFGEN comparison between the normalised intensity profiles $I(p)$ of Rigel in the H α line and its nearby continuum (dashed yellow and red lines, respectively), and the Bry line and its nearby continuum (solid green and blue lines, respectively) for the model with $\dot{M} = 8 \times 10^{-7} M_\odot \text{ yr}^{-1}$.

Figure 3 shows the computed theoretical visibility curves for Rigel across the Bry line with a mass-loss rate of $8 \times 10^{-7} M_\odot \text{ yr}^{-1}$. The corresponding differential visibility profiles are overlaid with the observed differential visibilities in Figs. B.3, C.3, and C.4 and in general provide a good match to the observations. However, the observed differential visibility profiles do show variations with respect to the steady-state model profiles either as red- or blue-shift of the visibility profile or variation in its width. By fitting Gaussian curves on the differential visibilities and the spectra, we estimated the position of the core of the visibility in the line, and the FWHM, in km s^{-1} . From December 2006 to March 2007, the core is blueshifted from about -20 km s^{-1} , moving to 0 km s^{-1} in March. The FWHM remains fairly constant, about $100 \pm 10 \text{ km s}^{-1}$. During that period of time, the spectral changes in the Bry line are more noticeable. We have an absorption peaking at 40 km s^{-1} in December 2006. In March 2007, the line is centred on the reference value, and exhibits symmetrical dips. The 2009–2010 period is much quieter compared to 2006–2007. The Bry visibility signal remains well-centred at zero velocity. This variability is indicative of large-scale inhomogeneities in the line forming region but will not be discussed any further here.

The visibilities measured in the core of the Bry line during 2009–2010 are well described by a uniform-disk diameter of 2.76 mas increased by 25%, corresponding to 3.45 ± 0.04 mas. For the 2006–2007 data set a uniform-disk diameter of 3.58 ± 0.04 mas is measured. Both determinations correspond to an extension of the Bry line forming region of $\sim 1.25 R_*$. Given the number of measurements and the error bars, the 4% difference in the extent of the Bry line-forming region between the two periods is significant.

Using CMFGEN and varying only the mass-loss rate parameter, we performed a fit of the differential visibilities for each triplet of baselines that are shown in Figs. B.3, C.3, and C.4. Bearing in mind the limited statistics, such an analysis yields a mass-loss rate of $9.4 \pm 0.9 \times 10^{-7} M_\odot \text{ yr}^{-1}$ and $7.6 \pm 1.1 \times 10^{-7} M_\odot \text{ yr}^{-1}$ for the 2006–2007 and 2009–2010 campaigns, respectively. This implies variations in mass-loss rate at a level of 20–25% over a period of several months. As discussed in Sect. 3, a change in the continuum diameter of Rigel between the two epochs is probable and would affect this analysis. Hence,

the estimated variations in mass-loss rate could even be underestimated when taking into account a change in the diameter of Rigel as a consequence of a variation in mass-loss rate.

Figure 4 illustrates the variation in the intensity as a function of impact parameter and for different selected wavelengths – the model used has a mass-loss rate of $8 \times 10^{-7} M_{\odot} \text{ yr}^{-1}$. This model predicts a larger uniform-disk diameter for $H\alpha$ than for $\text{Br}\gamma$. $H\alpha$ can probe structures up to 3 stellar radii while the $\text{Br}\gamma$ perturbations mostly originate at most at 1.5 stellar radii. Moreover, one expects the $\text{Br}\gamma$ perturbations to be brighter close to the photosphere because the $H\alpha$ emitting region is more extended. This difference must be kept in mind in the frame of the differential phase/photocentre analysis performed in Sect. 6. Using optical interferometric observations of Rigel, Chesneau et al. (2010) inferred a uniform-disk diameter of the $H\alpha$ line forming region of 4.2 mas, equivalent to $\sim 1.5 R_{*}$. However, the corresponding fit of the differential visibilities of $H\alpha$ required a much lower mass-loss rate of $1.5 \times 10^{-7} M_{\odot} \text{ yr}^{-1}$ than required for $\text{Br}\gamma$ in this study. Further work on the CMFGEN model, out of the scope of the present paper, is needed to solve this inconsistency.

6. Differential phases and circumstellar structures

Figures B.4, C.5, and C.6 show in the first three columns corresponding to the three available baselines the measured differential phases across the $\text{Br}\gamma$ line in the 2006–2007 and 2009–2010 data set, respectively. In some differential phase measurements of Rigel a statistically significant, non-zero signal is detected across the $\text{Br}\gamma$ line. The signal is highly complex (and noisy) across the line and reaches from typical values of ± 2 degrees to maximum values of -6 to $+8$ degrees. This observation of a non-zero interferometric signal in the differential phases across the $\text{Br}\gamma$ line is indicative of asymmetry of the line forming region and therefore the circumstellar envelope. Yet, the signal is also very weak, suggesting that the perturbation can only be considered as a second-order effect. As shown in Figs. B.2 and C.2, this corresponds also to moderate changes in the $\text{Br}\gamma$ line, never exceeding 10% of the line profile. The strongest differential phase signal can often be characterised by so-called S-shaped profiles (see e.g. Fig. C.5 at MJD 55 238) that are commonly interpreted as signatures of *rotating* circumstellar structures (see for instance Millour et al. 2013).

To further explore the nature and characteristics of Rigel’s circumstellar structures and their temporal variation in the absence of a detailed model that could be inverted to fit the measured differential phase, the measured differential phases ϕ are converted into differential astrometric shifts p using the well-known relation for marginally resolved interferometric observations (Lachaume 2003; Chelli & Petrov 1995)

$$p = -\frac{\phi}{2\pi} \cdot \frac{\lambda}{B} \quad (1)$$

where B is the projected baseline and λ is the wavelength of the spectral channel. p represents the projection in the baseline direction of the estimated 2D photocentre in the plane of the sky \mathbf{p} . With a triplet of baselines provided by a single observation with AMBER the astrometric solution (i.e. a single 2D vector \mathbf{p}) can be estimated reliably using a robust least-square minimisation scheme. Furthermore, this global fit is linear and can be performed at each wavelength through the $\text{Br}\gamma$ line. For a recent discussion on the relation between differential phases and photocentre shifts see Millour (2012).

However, Eq. (1) is formally only applicable to unresolved or marginally resolved objects with visibilities close to 1.

Table 2. Position angles and extensions of the structures measured in the photocentre shifts in Figs. B.4, C.5, and C.6.

2006–2007 campaign			
MJD	PA [°]	L [mas]	Comment
54 099.104	145	0.05	small loop
54 107.174	45	0.12	single-sided arm
54 108.058	50	0.12	single-sided arm
54 137.055	135	0.12	narrow loop
54 168.008	>135, <260	0.06, 0.08	wide loop
2009–2010 campaign			
MJD	PA [°]	L [mas]	Comment
55 139.263	>30, <160	0.06, 0.05	wide loop
55 152.258	<30, >200	0.06, 0.12	wide loop
55 189.175	–	<0.01	no structure
55 217.061	315	0.04	small loop
55 238.039	0, 205	0.05, 0.10	wide loop
55 267.037	–	–	could not be determined
55 275.084	–	–	undefined structures
55 299.986	200	0.07	single-sided arm

Therefore, the limitations of applying this method to more extended and resolved objects like Rigel must be carefully considered. With the longest baselines, the $\text{Br}\gamma$ line-forming region of Rigel is well resolved with observed visibilities in the range of 0.1 to 0.3 and hence the astrometric signal is biased. Such a bias is difficult to evaluate quantitatively without a good knowledge of the geometry of the source. Qualitatively, the bias results in a distortion of the reconstructed patterns. This distortion can be considered as a systematic bias in the 2006–2007 dataset because all observations have been obtained with the same telescope configuration, i.e. the UT1-3-4 triplet (see Table A.2).

The reconstructed photocentre shifts as a function of spectral channel across the $\text{Br}\gamma$ line of the Rigel data sets are shown in the right-most column of Fig. B.4 for the 2006–2007 dataset and in Figs. C.5 and C.6 for the 2009–2010 dataset. The black diamonds represent the continuum points measured outside the velocity intervals $\pm 40 \text{ km s}^{-1}$ centred on the line, the coloured diamonds represent the different wavelengths across the line.

The cloud of black diamonds in the centre of the figures are the continuum points that provide a good insight on the level of the formal error bar due to the statistical variations in the differential phases. Well-structured photocentre shifts for the spectral channels within the $\text{Br}\gamma$ line are observed at several epochs of the 2006–2007 and 2009–2010 campaigns. The patterns exhibit similar shapes, whether in the form of a weakly-curved single-sided arm connected to the star or in the form of loops indicative of a more complex velocity structure. The measured characteristics of the observed structures are summarised in Table 2.

Before discussing the observed extended structures it is worth noting that at MJD 55 189 *no* photocentre shifts larger than 0.01 mas corresponding to 0.4% of the stellar radius were observed indicating a mostly undisturbed, spherically symmetric envelope, i.e. a rather uncommon state of quiescence for Rigel. Unfortunately, no optical spectrum was recorded on the same night but the $H\alpha$ spectrum closest in time, i.e. on MJD 55 178 displays a classical P-Cygni line profile (see Fig. 2) with red-shifted emission and blue-shifted absorption, compatible with a spherical-symmetric stellar wind. It should be noted here that the observed photocentre shifts never exceed 0.12 mas corresponding to $1.04 R_{*}$, i.e. the observed structures to which the $\text{Br}\gamma$ lines is sensitive and which are described in the following are located very close to the star.

The first one-armed structure observed in the photocentre shifts in 2006–2007 on MJD 54 107 and 54 108 appears rather stable from one day to the next with a possible (counter-clock wise) increase in the position angle of a few degrees. Some 30 days later (MJD 54 137) the pattern seems to have rotated counter-clockwise by about 90 degrees. The pattern has also curved and has the appearance of a loop. Most of the signal is found in the blue side of the line, evolving from blue to red. Observations performed another 30 days later (MJD 54 168) are of lower quality as witnessed by the asymmetry of the continuum cloud of points (black diamonds). Yet, a significant differential signal is observed near the zero velocity, giving rise to a weak but significant arm whose angle seems to fit consistently into the counter-clockwise rotation observed before.

The timescale of 30 days for a quarter of a full rotation is consistent with the estimated upper limit for the stellar rotation period of 107 days (Kaufer et al. 1996b).

No such consistent pattern evolution is observed in the 2009–2010 campaign. At MJD 55 139, a complex, loopy pattern is observed. Unfortunately, at MJD 55 152, only one good quality differential phase was obtained, hampering the photocentre interpretation. At MJD 55 217, a small loop pattern is observed that develops at MJD 55 238 into an extended loop pattern that seems to extend in two almost opposite directions and therefore involves a large circumstellar volume.

The largest photocentre shift and the strongest observed S-shaped signal in the differential phases of the complete available data set was observed at MJD 55 238. This measurement connects with the strongest observed feature in the spectral time series in $H\alpha$, i.e. a comparatively weak HVA event becoming visible about 30 days later at MJD 55 264. Admittedly, the sequential appearance of the two features could be pure coincidence which can not be ruled out due to the lack of temporal sampling of the interferometric data set. However, since the time lag of 25 days can possibly be identified with one quarter of the estimated rotation period of Rigel (Kaufer et al. 1996b), it is possible that we observe the rotation of an extended circumstellar structure from next to the star (observable in the differential phase of $B\gamma$ through a photocentre shift) into the line of sight in front of the star (observable as blue-shifted absorption in the $H\alpha$ line profile).

7. Results and discussion

We interpret the $H\alpha$ and $B\gamma$ spectral variability as variable emission superimposed on expanding wind profiles. The 2006–2007 visibilities data set (in comparison with 2009–2010 data set) indicates an increased size of the photosphere and the $B\gamma$ forming region. We may speculate that such an increase linked to the large mass-ejection event seen at MJD 54048 (high-velocity absorption HVA in line of sight extending to -400 km s^{-1}). The CMFGEN modelling show that a mass-loss change of about 20% between the two epochs can explain the variation in the differential visibilities (see Figs. B.3, C.3, and C.4). We detected many occurrences in the differential phases in $B\gamma$ of some S-shaped signals indicative of rotating circumstellar material that also causes the spectral variation. Linking these differential phases to photocentre shifts by a linear relationship provides some evidence that these structures are extended, reminiscent of loops. The strongest S-shaped signal is observed in 2009–2010 data set around MJD 55 240. This event was not preceded between MJD 55 265 and MJD 55 280 (end of data set) by any strong features in $H\alpha$ followed by a strong absorption event crossing the $H\alpha$ line profile from -250 to $+150 \text{ km s}^{-1}$ nor by any strong

features in the interferometric signal at that time. The $B\gamma$ line-forming region being closer to the star than $H\alpha$, it is probable that the detection of the interferometric signal occurred shortly after the material ejection or wind perturbation.

The interferometric monitoring of such events shows that they occur at a low rate of 1–2 per year. The differential phases show that this ejection is *local*, from a defined location at the star surface. Elaborated hydrodynamical 2D and 3D models of CIRs were shown in Dessart (2004) and Dessart & Chesneau (2002). Theoretical expectations for interferometric observations of such a perturbed hot star outflow were proposed and it was shown that strong spectrally dispersed signal of the same nature as those determined from spectroscopy were present in the differential phases. Applying the same linear photocentre-shift relation used in this paper (and therefore being subject to similar biases) the theoretical signatures have the appearance of a loop or arm that rotates around the star. In their Figs. 11 and 12, Dessart & Chesneau (2002) showed the cumulative signal over a rotation period and its dependence on the star inclination. In the monitoring presented here, we are far from having the time and spatial coverage to compare to these plots, but one can note an encouraging resemblance. First the level of the signal, about 0.05 to 0.1 mas is comparable to the level shown in the theoretical study. Second, the appearance of the differential signal and its conversion into a photocentre shift is also similar. In the theoretical study of Dessart & Chesneau (2002), two perturbations were artificially included as the origin of two CIRs at each side of the star but only one pattern is observed at any one time around Rigel.

8. Conclusions

We have reported on the first optical interferometric campaign aiming at studying the activity observed around the bright blue supergiant star Rigel. The organisation of a long-term monitoring is challenging and imposes stringent constraints on the VLTI infrastructure to obtain as regularly as possible observations with a configuration of telescopes that optimally would be close to an equilateral triangle. In both campaigns, this condition could not be fulfilled due to the complexity of the telescope relocation management for this open facility. Furthermore, a spectral resolution of $R = 12\,000$ is required to resolve the $B\gamma$ line due to the small $v \sin i$ of Rigel. Only AMBER/VLTI in the southern hemisphere and VEGA/CHARA in the northern hemisphere can currently perform such a challenging and demanding temporal monitoring.

The results obtained are promising. It has been shown that the $B\gamma$ line-forming region is well resolved by the interferometer. CMFGEN modelling implies a mass-loss rate at least a factor two larger than in the very similar model published by Chesneau et al. (2010) to account for the VEGA/CHARA interferometric observations in the $H\alpha$ line. It is out of the scope of this paper to investigate further the origin of such a discrepancy. However, these observations illustrate the need for a global approach to obtain robust models of B supergiant photospheres and winds. The extent of the $B\gamma$ line-forming region was established at about $1.25 R_*$ but also found to be variable. This variability translates into mass-loss rate variations of at least 20% on a timescale of one year.

Strong activity is observed in the differential and closure phase, although at a low level. At some periods, no phase signal was observed at all. This confirms that the observed circumstellar activity is better understood in the context of second-order

perturbations of an underlying spherically wind whose properties can be well reproduced by a 1D radiative transfer code.

The phase signal is spectrally extended, implying a large physical extent of the perturbation. The observed temporal variations suggest slowly evolving structures. This behaviour cannot be explained by the random emission of large scale clumps. Instead, the differential phases resemble the signal expected from theoretical models of CIRs. The well-structured signal implies that the activity around Rigel is very low, with some moderate eruptions occurring at a month to years timescale. The detected structures can be followed in the Bry line over 2–4 months, i.e. typically on a rotation timescale.

These conclusions are in line with results from numerous intense spectroscopic monitoring campaigns that have to date been performed on Rigel and other massive hot supergiants.

Acknowledgements. We thank J. B. LeBouquin and Ph. Berio for their help with the photocentre inversion. This publication is supported as a project of the Nordrhein-Westfälische Akademie der Wissenschaften und der Künste in the framework of the academy programme by the Federal Republic of Germany and the state Nordrhein-Westfalen.

References

- Aerts, C., Puls, J., Godart, M., & Dupret, M. 2009, *A&A*, 508, 409
- Aufdenberg, J. P., Ludwig, H., Kervella, P., et al. 2008, in *The Power of Optical/IR Interferometry: Recent Scientific Results and 2nd Generation*, eds. A. Richichi, F. Delplancke, F. Paresce, & A. Chelli, ESO Astrophysics Symposia (Springer), 71
- Bordé, P., Coudé du Foresto, V., Chagnon, G., & Perrin, G. 2002, *A&A*, 393, 183
- Chelli, A., & Petrov, R. G. 1995, *A&AS*, 109, 389
- Chesneau, O., Dessart, L., Mourard, D., et al. 2010, *A&A*, 521, A5
- Cranmer, S. R., & Owocki, S. P. 1996, *ApJ*, 462, 469
- Dessart, L. 2004, *A&A*, 423, 693
- Dessart, L., & Chesneau, O. 2002, *A&A*, 395, 209
- Dessart, L., & Hillier, D. J. 2005, *A&A*, 437, 667
- Dessart, L., & Owocki, S. P. 2002, *A&A*, 383, 1113
- Dessart, L., & Owocki, S. P. 2005, *A&A*, 437, 657
- Fuhrmann, K., Chini, R., Hoffmeister, V. H., et al. 2011, *MNRAS*, 411, 2311
- Gilheany, S. 1991, *Vist. Astron.*, 34, 249
- Hillier, D. J., & Miller, D. L. 1998, *ApJ*, 496, 407
- Howarth, I. D., Prinja, R. K., & Massa, D. 1995, *ApJ*, 452, L65
- Kaufer, A., Stahl, O., Wolf, B., et al. 1996a, *A&A*, 314, 599
- Kaufer, A., Stahl, O., Wolf, B., et al. 1996b, *A&A*, 305, 887
- Kaufer, A., Stahl, O., Wolf, B., et al. 1997, *A&A*, 320, 273
- Kaufer, A., Stahl, O., Tubbesing, S., et al. 2000, in *Optical and IR Telescope Instrumentation and Detectors*, eds. M. Iye, & A. F. Moorwood, *Proc. SPIE*, 4008, 459
- Kaufer, A., Stahl, O., Prinja, R. K., & Witherick, D. 2006, *A&A*, 447, 325
- Lachaume, R. 2003, *A&A*, 400, 795
- LeBouquin, J. B., Rousselet-Perraut, K., Kern, P., et al. 2004, *A&A*, 424, 719
- Lefever, K., Puls, J., & Aerts, C. 2007, *A&A*, 463, 1093
- Markova, N., Prinja, R. K., Markov, H., et al. 2008, *A&A*, 487, 211
- Massa, D., Fullerton, A. W., Nichols, J. S., et al. 1995, *ApJ*, 452, L53
- Millour, F. 2012, in *ASP Conf. Ser. 464*, eds. A. C. Carciofi, & T. Rivinius, 15
- Millour, F., Meilland, A., Stee, P., & Chesneau, O. 2013, in *Lect. Notes Phys.* 857, eds. J.-P. Rozelot, & C. Neiner (Berlin Springer Verlag), 149
- Moravveji, E., Guinan, E. F., Shultz, M., Williamson, M. H., & Moya, A. 2012a, *ApJ*, 747, 108
- Moravveji, E., Moya, A., & Guinan, E. F. 2012b, *ApJ*, 749, 74
- Mourard, D., Clausse, J. M., Marcotto, A., et al. 2009, *A&A*, 508, 1073
- Petrov, R. G., Malbet, F., Weigelt, G., et al. 2007, *A&A*, 464, 1
- Prinja, R. K., Massa, D., & Fullerton, A. W. 1995, *ApJ*, 452, L61
- Prinja, R. K., Stahl, O., Kaufer, A., et al. 2001, *A&A*, 367, 891
- Przybilla, N., Butler, K., Becker, S. R., & Kudritzki, R. P. 2006, *A&A*, 445, 1099
- Rivinius, T., Stahl, O., Wolf, B., et al. 1997, *A&A*, 318, 819
- Rothman, L. S., Gamache, R. R., Tipping, R. H., et al. 1992, *J. Quant. Spectr. Rad. Transf.*, 48, 469
- Schnerr, R. S., Henrichs, H. F., Neiner, C., et al. 2008, *A&A*, 483, 857
- Shultz, M., Wade, G. A., Neiner, C., et al. 2011, in *IAU Symp. 272*, eds. C. Neiner, G. Wade, G. Meynet, & G. Peters, 212
- Simón-Díaz, S., Herrero, A., Uytterhoeven, K., et al. 2010, *ApJ*, 720, L174
- Stahl, O., Kaufer, A., & Tubbesing, S. 1999, in *Optical and Infrared Spectroscopy of Circumstellar Matter*, *ASP Conf. Ser.*, 188, 331
- Tatulli, E., Millour, F., Chelli, A., et al. 2007, *A&A*, 464, 29

Appendix A: Observation logs

Table A.1. Observation log of the FEROS and BESO observations of Rigel.

2006–2007 campaign with FEROS							
Spectrum	Date	MJD	<i>n</i>	Spectrum	Date	MJD	<i>n</i>
1	2006-Oct-03	54 011.36031973	6	11	2006-Dec-27	54 096.31590096	5
2	2006-Oct-07	54 015.28385735	6	12	2007-Jan-01	54 101.16567652	36
3	2006-Oct-11	54 019.36730933	3	13	2007-Jan-17	54 117.14069429	3
4	2006-Oct-29	54 037.31208022	20	14	2007-Feb-05	54 136.05338341	10
5	2006-Dec-02	54 071.25872330	6	15	2007-Feb-11	54 142.10571373	6
6	2006-Dec-05	54 074.30587822	5	16	2007-Feb-16	54 147.06192037	9
7	2006-Dec-08	54 077.19925441	13	17	2007-Feb-22	54 153.09321235	10
8	2006-Dec-14	54 083.17843854	10	18	2007-Mar-24	54 183.99706054	6
9	2006-Dec-18	54 087.28252888	6	19	2007-Mar-30	54 189.02635471	3
10	2006-Dec-22	54 091.14807436	11	20	2007-Mar-31	54 191.00199574	3
2009–2010 campaign with BESO							
Spectrum	Date	MJD		Spectrum	Date	MJD	
1	2009-Oct-06	55 110.33170140		41	2010-Feb-23	55 250.00540509	
2	2009-Oct-17	55 121.23127315		42	2010-Feb-24	55 251.02425926	
3	2009-Oct-20	55 124.26278935		43	2010-Feb-25	55 252.09684028	
4	2009-Oct-22	55 126.24055556		44	2010-Feb-26	55 253.04282407	
5	2009-Oct-24	55 128.23674768		45	2010-Feb-28	55 255.02221065	
6	2009-Oct-28	55 132.21540509		46	2010-Mar-01	55 256.00712963	
7	2009-Oct-30	55 134.27407408		47	2010-Mar-03	55 258.00199074	
8	2009-Nov-02	55 137.19428241		48	2010-Mar-05	55 260.99156253	
9	2009-Nov-04	55 139.18910879		49	2010-Mar-06	55 261.98248839	
10	2009-Nov-13	55 148.16081018		50	2010-Mar-07	55 262.98533567	
11	2009-Nov-15	55 150.14854167		51	2010-Mar-08	55 263.98876158	
12	2009-Nov-17	55 152.20844907		52	2010-Mar-09	55 264.98519675	
13	2009-Nov-19	55 154.20519676		53	2010-Mar-10	55 265.97914354	
14	2009-Nov-21	55 156.16405093		54	2010-Mar-13	55 268.00694444	
15	2009-Dec-01	55 166.28560185		55	2010-Mar-14	55 269.02199074	
16	2009-Dec-05	55 170.08598379		56	2010-Mar-14	55 269.97369210	
17	2009-Dec-09	55 174.17329862		57	2010-Mar-15	55 270.99855328	
18	2009-Dec-11	55 176.15767361		58	2010-Mar-16	55 271.98635419	
19	2009-Dec-13	55 178.09023148		59	2010-Mar-17	55 272.97731479	
20	2010-Jan-12	55 208.06005787		60	2010-Mar-18	55 273.98398145	
21	2010-Jan-12	55 208.06197916		61	2010-Mar-20	55 275.01642361	
22	2010-Jan-14	55 210.05552083		62	2010-Mar-22	55 277.05741898	
23	2010-Jan-16	55 212.05674768		63	2010-Mar-22	55 277.99923611	
24	2010-Jan-18	55 214.05457176		64	2010-Mar-23	55 278.97440974	
25	2010-Jan-18	55 214.05793981		65	2010-Mar-25	55 280.05094907	
26	2010-Jan-22	55 218.10179398		66	2010-Mar-25	55 280.96922453	
27	2010-Jan-25	55 221.02671296		67	2010-Mar-26	55 281.97070599	
28	2010-Jan-29	55 225.14851852		68	2010-Mar-27	55 282.96931712	
29	2010-Jan-31	55 227.12858796		69	2010-Mar-28	55 283.96629628	
30	2010-Feb-05	55 232.02315972		70	2010-Mar-29	55 284.97012734	
31	2010-Feb-08	55 235.00275463		71	2010-Mar-30	55 285.98187502	
32	2010-Feb-10	55 237.06417824		72	2010-Mar-31	55 286.98141201	
33	2010-Feb-12	55 239.10770833		73	2010-Apr-01	55 287.97542826	
34	2010-Feb-14	55 241.11258101		74	2010-Apr-02	55 288.97332176	
35	2010-Feb-16	55 243.01336806		75	2010-Apr-03	55 289.97159719	
36	2010-Feb-18	55 245.03077546		76	2010-Apr-04	55 290.96679401	
37	2010-Feb-19	55 246.00457176		77	2010-Apr-05	55 291.97576388	
38	2010-Feb-19	55 246.99271989		78	2010-Apr-07	55 293.00043981	
39	2010-Feb-21	55 248.00678241		79	2010-Apr-07	55 293.99209491	
40	2010-Feb-22	55 249.04751157					

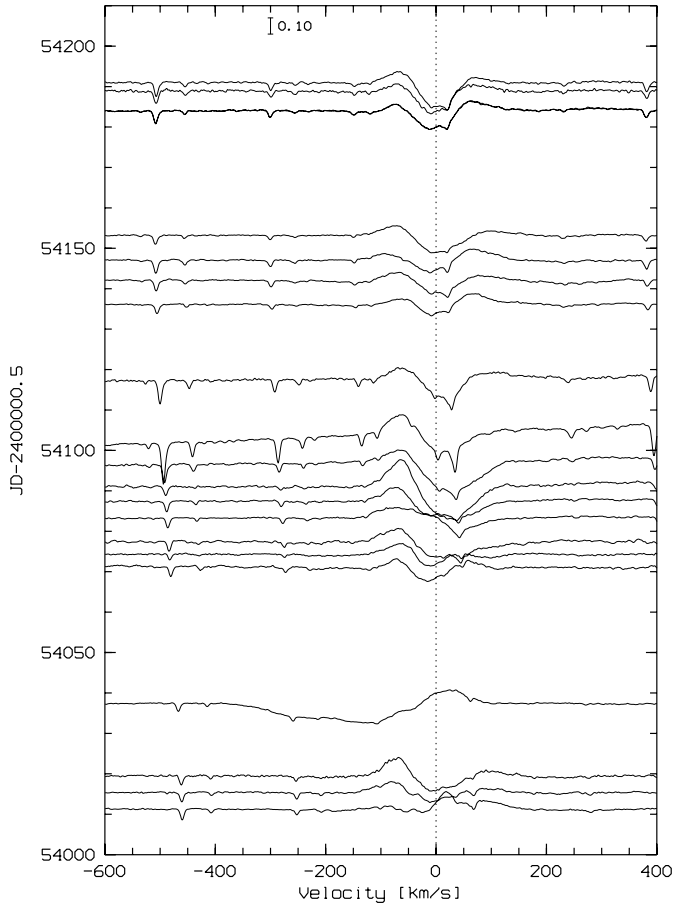
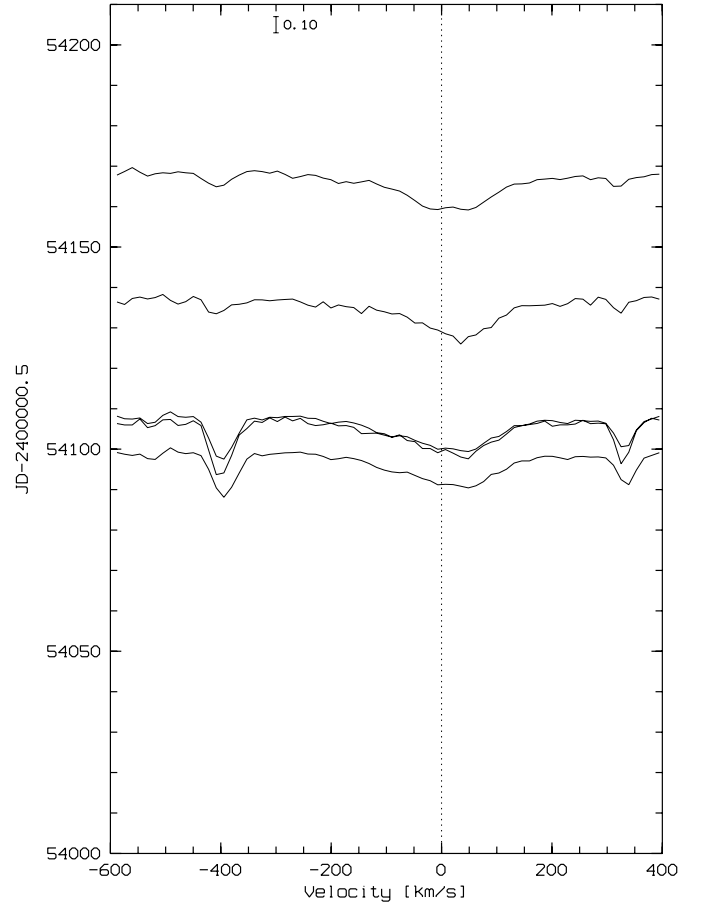
Notes. Column *n* indicates the number of spectra that have been combined from the respective night.

Table A.2. Observation log of AMBER.

2006–2007 campaign with AMBER									
Spectrum	Date	MJD	Stations	Length [m]			PA [degrees]		
1	2006-Dec-30	54 099.104	UT1–3–4	96.4	62.2	123.8	28.8	108.3	58.4
2	2007-Jan-07	54 107.174	UT1–3–4	102.4	56.5	127.9	38.8	115.4	64.2
3	2007-Jan-08	54 108.058	UT1–3–4	94.1	61	118.5	25.0	107.6	55.7
4	2007-Feb-05	54 137.055	UT1–3–4	101.1	60.7	130.1	36.0	111.7	62.9
5	2007-Mar-08	54 168.008	UT1–3–4	102.4	55.5	126.8	39.1	116.2	64.3
2009–2010 campaign with AMBER									
Spectrum	Date	MJD	Stations	Length [m]			PA [degrees]		
1	2009-Nov-04	55 139.263	UT1–3–4	97.3	62.4	135.5	30.2	108.7	59.4
2	2009-Nov-04	55 139.279	UT1–3–4	98.4	62.4	127.5	31.9	109.3	60.4
3	2009-Nov-17	55 152.258	A0–K0–G1	87.9	89.4	127.7	–152.0	–64.4	–107.0
4	2009-Dec-24	55 189.175	A0–K0–G1	88.8	87.8	127.8	–150.0	–63.1	–107.0
5	2010-Jan-21	55 217.061	A0–K0–G1	86.4	90.4	125.7	–155.0	–65.9	–109.0
6	2010-Feb-11	55 238.039	A0–K0–G1	88.7	88.0	127.9	–150.0	–63.3	–107.0
7	2010-Mar-12	55 267.037	D0–H0–K0	56.5	28.2	84.8	74.8	74.8	74.8
8	2010-Mar-20	55 275.084	A0–K0–G1	86.0	53.8	78.9	–145	–29	–107
9	2010-Apr-13	55 299.986	D0–I1–G1	53.5	43.3	55.4	114.5	–134	161.3

Notes. The projected baselines at the dates of observation are provided in length and position angle (PA).

Appendix B: 2006–2007 campaign

**Fig. B.1.** 2006–2007 H α time series of Rigel obtained with FEROS.**Fig. B.2.** 2006–2007 Bry time series of Rigel obtained with AMBER.

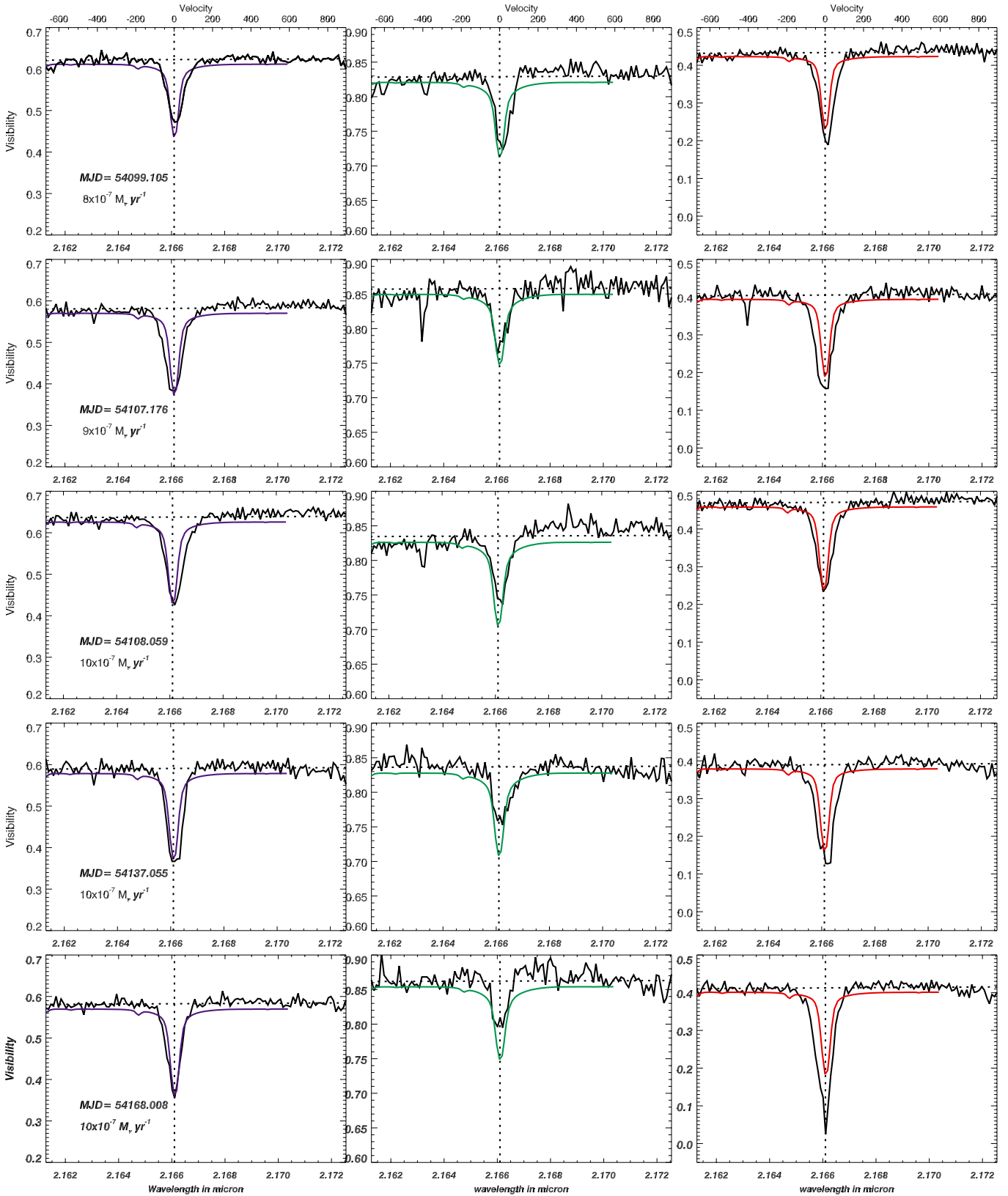


Fig. B.3. Differential visibilities of Rigel obtained in 2006–2007 and put to the scale corresponding to an angular diameter of 2.75 mas. The visibilities are compared with the ones computed from CMFGEN models tuning the mass-loss rate only.

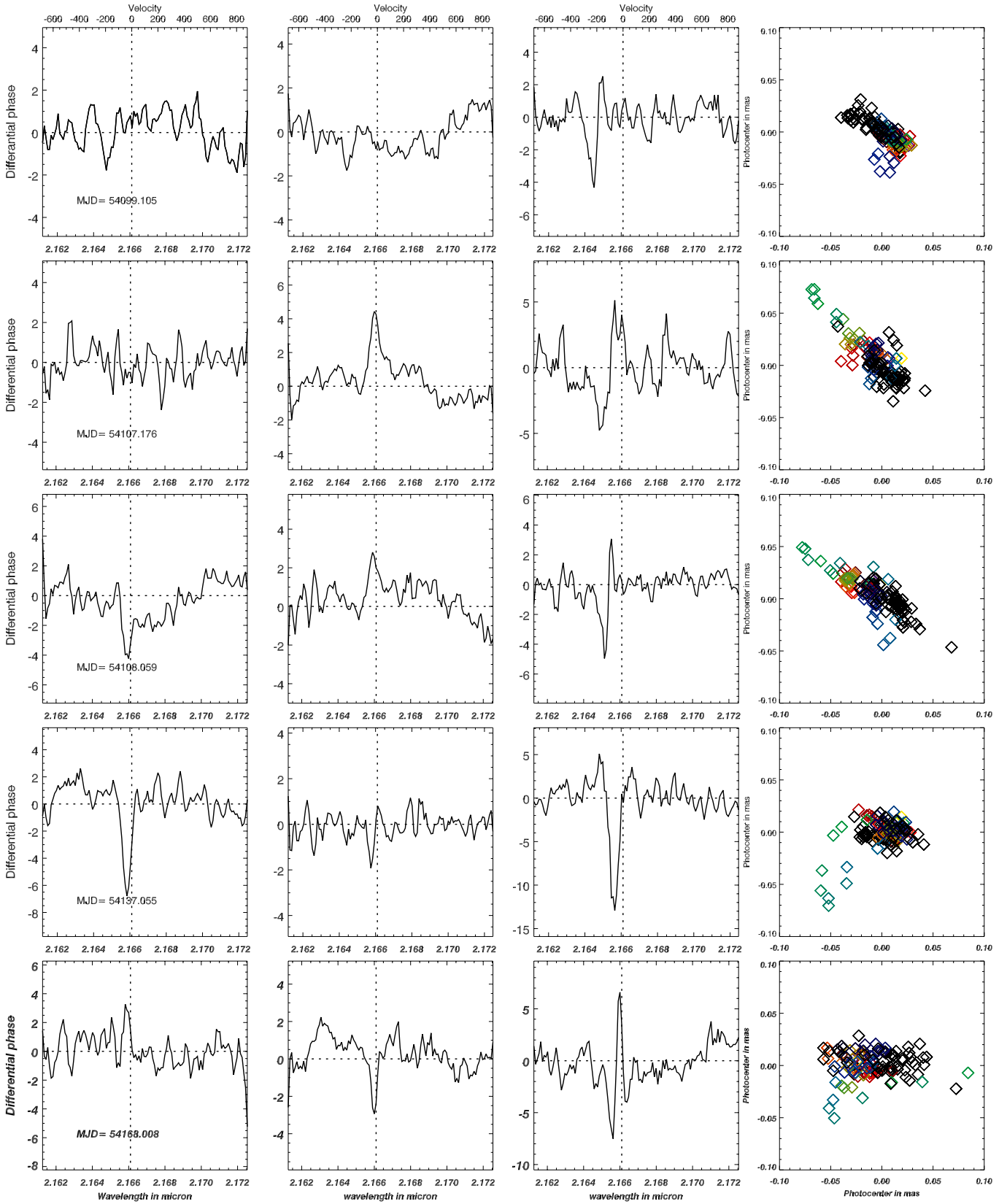


Fig. B.4. Differential phases and photocenter shift of Rigel obtained in 2006–2007.

Appendix C: 2009–2010 campaign

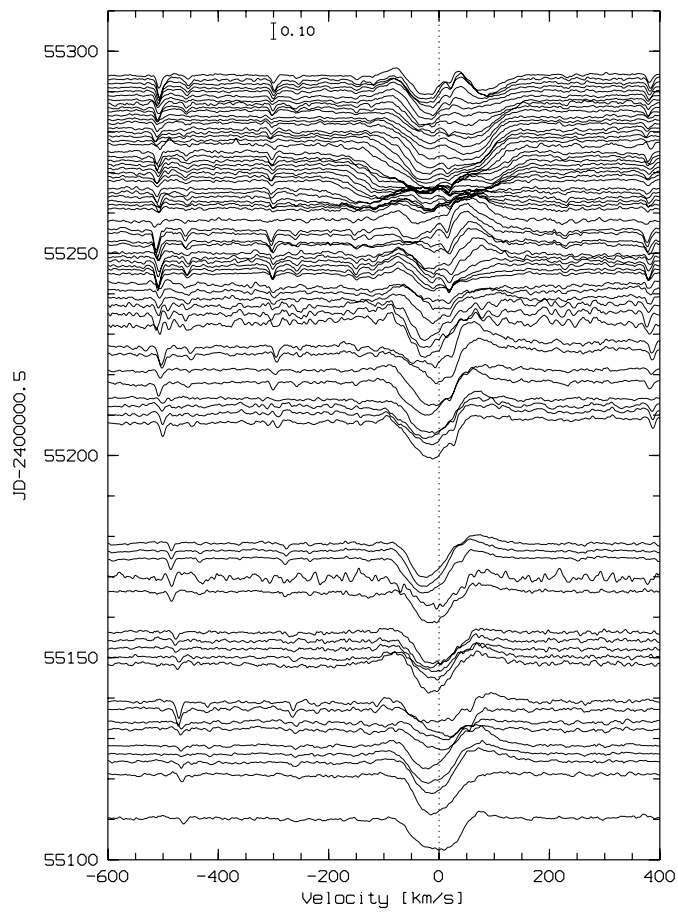


Fig. C.1. 2009–2010 H α time series of Rigel obtained with BESO.

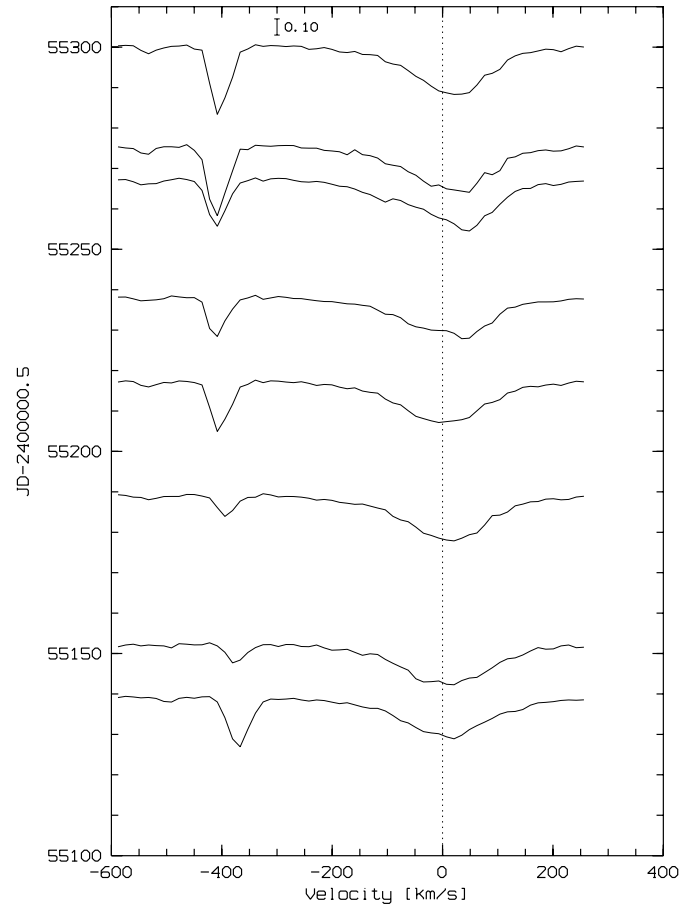


Fig. C.2. 2009–2010 Bry time series of Rigel obtained with AMBER.

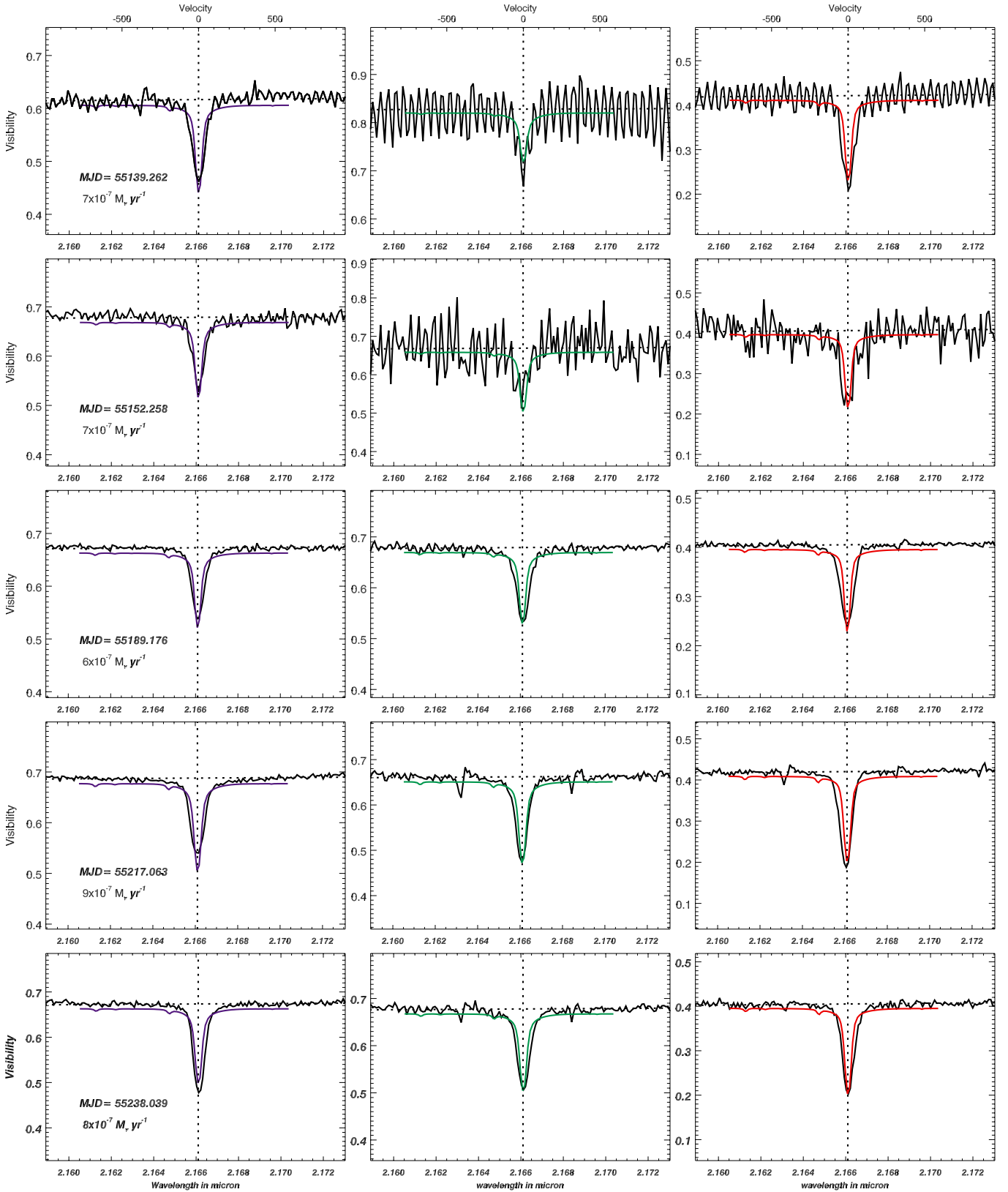


Fig. C.3. Differential visibilities of Rigel obtained in 2009–2010 and put to the scale corresponding to an angular diameter of 2.75 mas. The visibilities are compared with the ones computed from CMFGEN models with varying mass-loss rate.

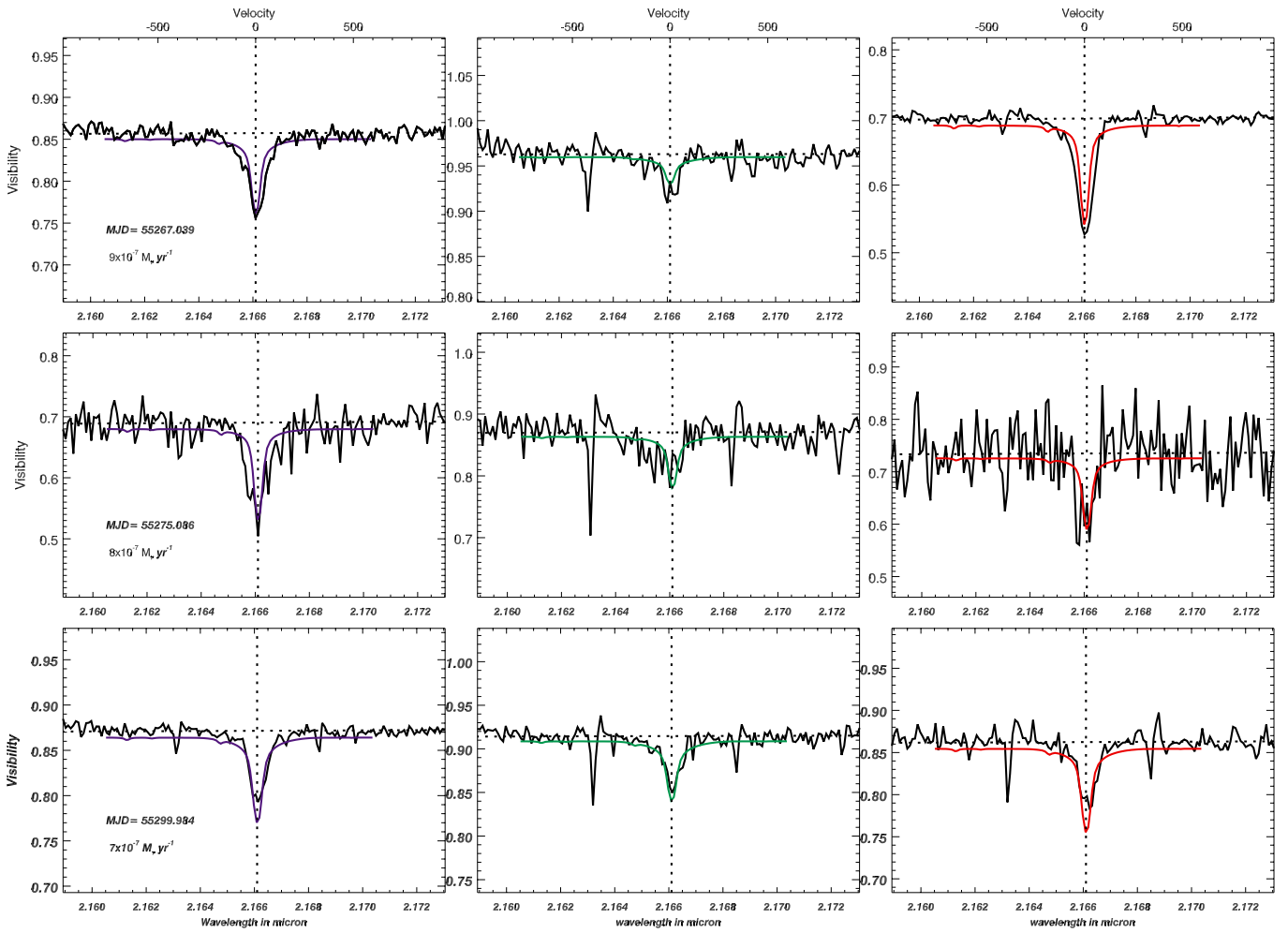


Fig. C.4. Differential visibilities of Rigel obtained in 2009–2010 (continued).

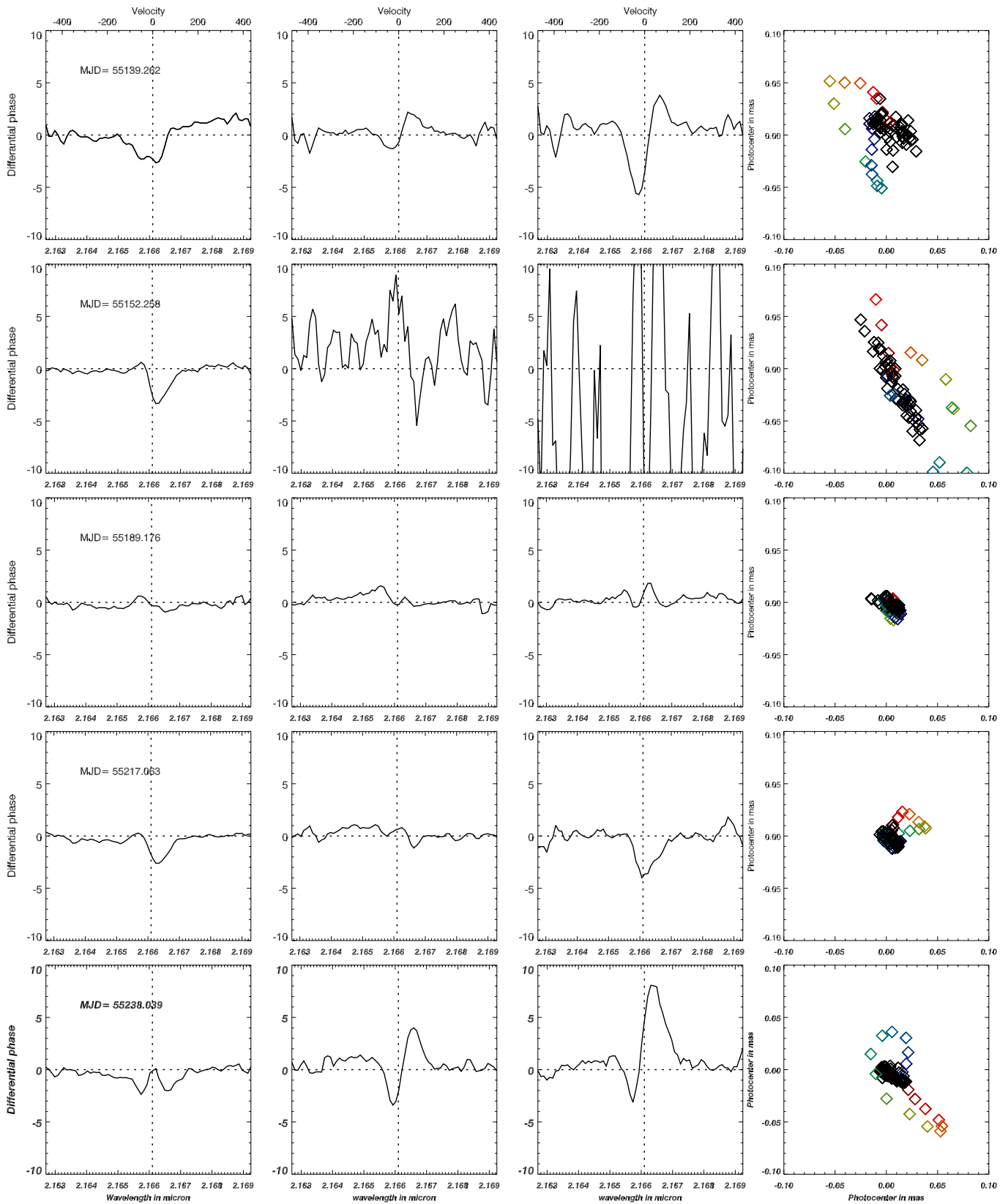


Fig. C.5. Differential phases and photocenter shift of Rigel obtained in 2009–2010.

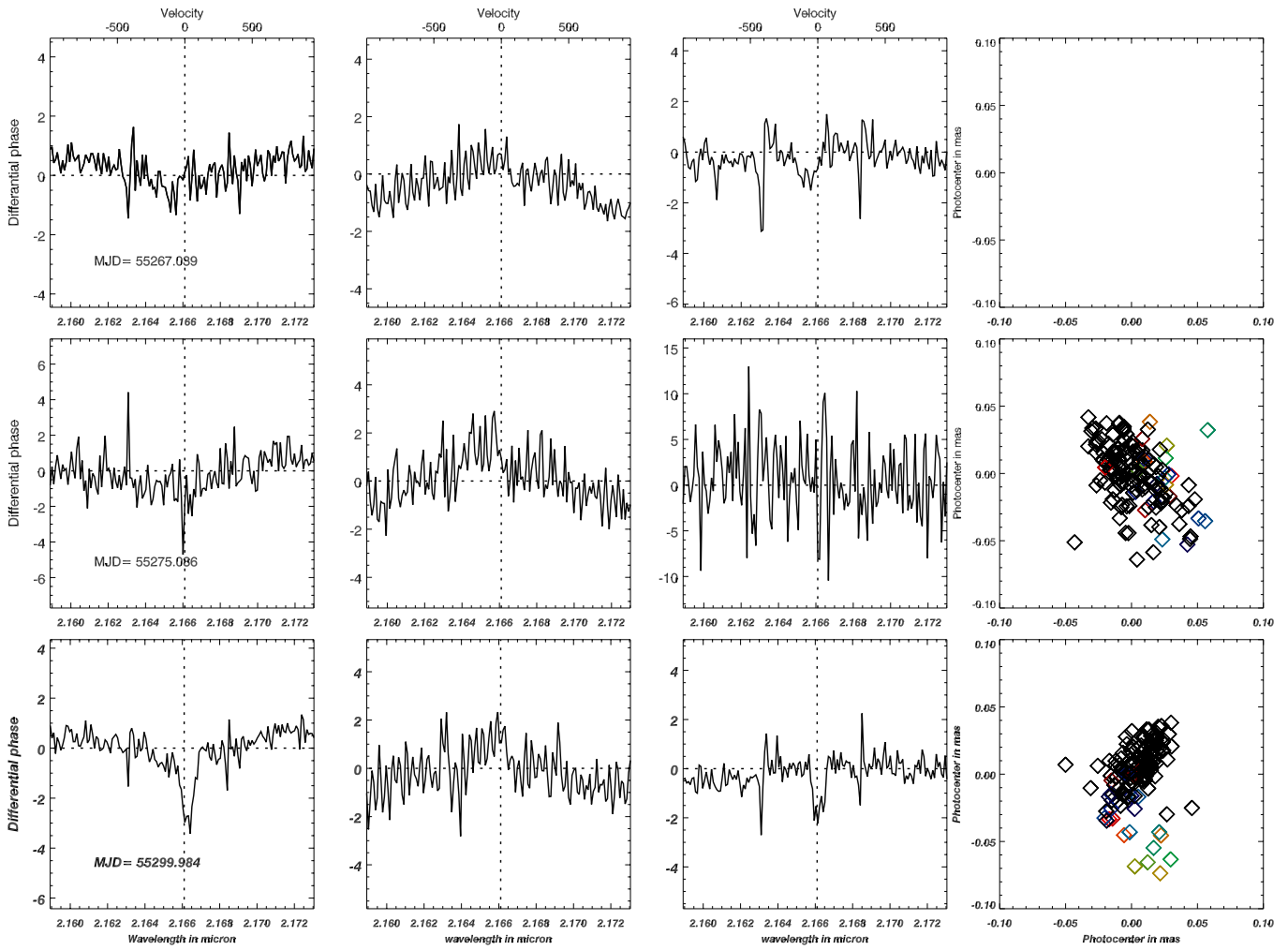


Fig. C.6. Differential phases and photocentre shift of Rigel obtained in 2009–2010 (continued). At MJD = 55 267.099 (*upper row*), the baselines were aligned preventing the computation of a 2D photocentre.